JOURNAL OF GEOPHYSICAL RESEARCH, VOL. 88, NO. A12, PAGES 10,170-10,188, DECEMBER 1, 1983

A REVISED THERMOSPHERIC MODEL BASED ON MASS SPECTROMETER AND INCOHERENT SCATTER DATA: MSIS-83

A. E. Hedin

Planetary Aeronomy Branch, Goddard Space Flight Center

Abstract. The MSIS-83 empirical model of temperature, density and composition is a revision of the original MSIS model (including longitude/UT effects) and is based on temperature, density, and composition data from a comprehensive summary of rocket flights, seven satellites, and five incoherent scatter radars, including data from high solar activity. The model extends the previous description of neutral parameters to the base of the thermosphere in a continuous manner while maintaining the basic structure of the MSIS model at higher altitudes. As the altitude decreases, composition approaches lower atmosphere values, while yearly, and to a lesser extent daily, variations in temperature and density are in reasonable agreement with previous results for the lower thermosphere. An alternate description of magnetic storm variations is provided based on the three hour ap indices and an 8- to 10-hour exponential decay in thermospheric density and temperature response after a heating event. Additional coefficients are included for the time independent and magnetic activity terms, including a longitudinally dependent seasonal magnetic activity effect. The molecular oxygen description is based on mass spectrometer and EUV absorption measurements rather than ion chemistry.

1. Introduction

The MSIS model of thermospheric temperature and density [Hedin et al., 1977a,b] resulted from the joining of several incoherent scatter radar data sets, providing temperatures at specific latitudes, with several satellite mass spectrometer data sets providing composition on a global basis. The combined data sets were successfully represented using the formalism of the OGO 6 model [Hedin et al., 1974] and provided a more accurate representation of composition and temperature than available in the Jacchia [1971] satellite drag based model, while reaching reasonable agreement in total density with the drag based model.

Several limitations of the MSIS model are apparent. While data taken under low to moderate solar activity conditions are well represented in the model, there are few data from high solar activity conditions ($F_{10.7} > 170$). A formal limitation of the MSIS model is the lower boundary at 120 km, which has no particular physical significance. The dependence of O_2 variations on ion measurements and chemistry considerations compromised the character of the model as an independent input to aeronomic calculations.

This paper presents a revised model (designated MSIS-83) with the goal of covering the entire thermosphere (above 85 km) as well as a wide range of solar activities (from $F_{10.7} = 70$ to over 200). The model maintains the basic structure of the MSIS model above 120 km, as augmented by longitude/UT effects [Hedin et al., 1979], for diffusive equilibrium profiles, except that it uses the temperature gradient at 120 km as a fitting parameter rather than the Bates [1959] shape (s) parameter. The temperature profile below 116.5 km is an inverse polynomial in geopotential height, and for densities there is a smooth transition to a mixing profile. In addition to the representation of magnetic storm effects using the daily magnetic index Ap, as in the MSIS model, an alternate representation is given using 3 hour ap indices in a formula based on a simplification of those presented by Porter et al. [1981]. Unlike the MSIS model, the molecular oxygen modeling is based on direct measurements by mass spectrometer and atmospheric absorption of EUV rather than derived from chemistry considerations. The new data base comprises data from seven satellites, five incoherent scatter stations, and a comprehensive summary of rocket probe data. Included in the expanded data base are in situ temperature and much new composition data from the Atmospheric Explorers, composition data from ESRO 4, temperature data from the Malvern incoherent scatter station and new data from Millstone Hill and Arecibo.

2. Data Selection

The data sets used in this study and references thereto are given in Table 1, which also indicates the approximate altitude coverage of the data and which data were used previously in MSIS. Unlike the original MSIS model, no averaging or smoothing was applied and no adjustments were made in absolute values.

Composition data gathered by rocket mass spectrometer and EUV absorption measurements were taken from the summary by Offermann [1974] and augmented, if possible, from the references cited therein plus data from Ackerman et al. [1974], Cooley and Reber [1969], and Trinks et al. [1978]. Derivation of temperature from the N_2 profiles assuming hydrostatic equilibrium is straightforward, for example, as carried out routinely by Spencer et al. [1969], and this was done with all the N_2 profiles which did not have temperatures reported by the original authors. A comprehensive summary (with original literature citations) of total density and (molecular) temperature data, from rocket-borne pressure gauge, grenade, and falling sphere measurements which reach up to the lower thermosphere have been reported by Minzner et al. [1967] and Theon et al. [1972] and these were used in the form

Paper number 3A1405.

TABLE 1. Data Sources for MSIS-83

Data Set	Measurement Altitudes, km	Nominal	References
OGO 6 (MS)[a]	N_2, O, He	400-700	Carignan and Pinkus [1968] Hedin et al. [1974]
San Marco 3 (MS)[a]	N_2, O, He, Ar	160-250	Newton et al. [1974] Newton et al. [1975]
Aeros-A NATE (MS)[a]	N_2, O, He, Ar	200-500	Spencer et al. [1974] Chandra and Spencer [1975]
AE-C NATE (MS)[b]	N_2, O, He, Ar	250-400	Spencer et al. [1973]
AE-C NATE (MS)[c]	Tp	135-300	Spencer et al. [1973]
AE-C OSS (MS)[d]	N_2, O, He, Ar, O_2	140-400	Nier et al. [1973] Nier et al. [1976]
AE-C BIMS (IMS)[b]	H	200-500	Brinton et al. [1973] Brinton et al. [1975]
AE-C MIMS (IMS)[c]	H	160-300	Breig et al. [1976]
AE-C EUVS (absorp)[c]	O_2	100-150	Hinteregger et al. [1973] Hinteregger and Chaikin [1977]
AE-D OSS (MS)[d]	N_2, O, He, Ar, O_2	140-400	(see AE-C OSS)
AE-D NATE (MS)[c]	Tp	140-400	(see AE-C NATE)
AE-E NACE (MS)[c]	N_2, O, He, Ar	140-450	Pelz et al. [1973]
AE-E NATE (MS)[c]	Tp	140-400	(see AE-C NATE)
AE-E OSS (MS)[c]	O_2	140-220	(see AE-C OSS)
AE-E BIMS (IMS)[c]	H	200-500	(see AE-C BIMS)
AE-E EUVS (absorption)[c]	O_2	100-150	(see AE-C EUVS)
ESRO 4 (MS)[c]	N_2, O, He, Ar	200-350	Trinks and von Zahn [1975] von Zahn et al. [1977] Jacchia et al. [1977] Laux and von Zahn [1979]
Rockets (MS)[c]	N_2, Ar, O_2, Tp	100-300	(see text)
Rockets (absorption)[c]	O_2	120-150	(see text)
Rockets (gauge)[c]	Rho, Tp	85-130	(see text)
Rockets (falling sphere)[c]	Rho, Tp	85-120	(see text)
Rockets (grenade)[c]	Rho, Tp	85-110	(see text)
Millstone Hill (IS)[c]	Tp	100-130	Salah and Evans [1973]; Oliver [1980]; Wand [1983a]; Wand [1983b]
Millstone Hill (IS)[b]	Tp	(exospheric)	
St. Santin (IS)[a]	Tp	(exospheric)	Alcayde [1974]
Arecibo (IS)[b]	Tp	(exospheric)	Waldteufel and Cogger [1971];
Arecibo (IS)[c]	Tp, N_2	100-135	Harper and Wand [1978]
Jicamarca (IS)[a]	Tp	(exospheric)	McClure [1971]
Malvern (IS)[c]	Tp	240-400	Williams and Taylor [1974] McPherson and Rishbeth [1979]

Tp: neutral temperature either measured directly or indirectly from ion temperature; Rho: total mass density; MS: neutral mass spectrometer; IMS: ion mass spectromter; IS: incoherent scatter.

[a] Essentially as used previously in MSIS.
[b] Partially used in MSIS.
[c] Not used at all in MSIS.
[d] O_2 not used in MSIS.

gathered on magnetic tape by R. A. Minzner (private communication).

While there is an element of redundancy in using temperatures derived from density profiles (or in some cases the inverse situation), it was felt that since only a sampling of data rather than complete profiles was used in the model generation, the complementary information was useful. As in the MSIS model, subsets of data were formed by random selection from all the data after sorting into boxes based on latitude, local time, day of year, UT, Ap, $F_{10.7}$, and altitude. In general, fitting was done with approximately four to five thousand data points at a time, which greatly exceed the number of coefficients to be determined.

3. Model Generation

The model formulation (see appendix for details) is based on a Bates [1959] temperature profile as a function of geopotential height for the upper thermosphere and an inverse polynomial in geopotential height for the lower thermosphere (equation (A1)) joined at 116.5 km (z_a) matching temperature and temperature gradient (equations (A2) and (A3)). These temperature profiles allow exact integration of the hydrostatic equation for a constant mass [e.g., Walker, 1965] (equations (A13) and (A14)) to determine a density profile based on a density (n_z) specified at 120 km as a function of geographical and solar/magnetic parameters. This approach to altitude profiles

is similar to that recently employed by Alcayde [1981]. The exospheric temperature T_∞, temperature T_ℓ, and temperature gradient T_ℓ' at 120 km, temperature T_o, and altitude z_o of the mesopause minimum, and the shape (as specified by the temperature T_{12}, halfway between z_o and z_a) of the lower thermospheric region are all expressed as functions of geographical and solar/magnetic parameters. The single altitude for joining the temperature profiles (z_a) was determined by fitting the data.

The transition from mixing to diffusive equilibrium near 105 km is handled in a manner similar to that used for Venus by Hedin et al. [1983], where net density is expressed as a root of the sum of diffusive and mixing densities each raised to a power (equation (A12)). Differentiation of this equation was shown to produce an analog to the differential equation often used in calculating altitude profiles based on eddy and molecular diffusion coefficients including a correction term C_1 for vertical flow. This approach supersedes use of the "u" coefficient term in MSIS, which could not be readily extended to lower altitudes.

The density coefficients at 120 km, as in MSIS, provide effective densities for calculating diffusive equilibrium profiles. The net density at 120 km, formed by combining diffusive and mixing profiles as described above, should be more representative of the real atmosphere than in MSIS.

The density profiles for mixing conditions are calculated using the mean molecular weight for the lower atmosphere while assuming that the diffusive and mixing profiles are equal at the turbopause. The turbopause height z_h was rounded off to 105 km for N_2, O_2, Ar, and O, 100 km for He, and 95 km for H from the calculations by Reber et al. [1976] for the U.S. Standard Atmosphere. A more precise or variable specification of the turbopause height was not believed justified at this time since there is so little actual data on composition in the transition region and there is essentially no effect on N_2 or total density. The most critical empirical constraints are the known mixing ratios Ω below the turbopause, and these are achieved by (A20b), where vertical flows are explicitly selected to provide the desired density ratios. A similar flow related correction factor is used by Reber et al. [1976] with the flow empirically selected to match mesopause and upper thermosphere densities.

It should be noted in connection with this formulation of the diffusion to mixing transition problem that it would be quite straightforward to include any specified variation of the turbopause height based on independent information or even indirectly based on specified eddy mixing coefficients. Furthermore, more than one term similar to (A20) could be used to specify vertical flow based on a particular geophysical variation. For example, there could be explicitly defined factors for annual variations and diurnal variations.

An additional flow term (equation (A21)) is used with atomic oxygen and hydrogen to reproduce the peak in their respective profiles in the lower thermosphere. The shape of the oxygen profile was guided by the U.S. Standard Atmosphere and the hydrogen profile by results of Liu and Donahue [1974] and Anderson et al. [1980]. No attempt was made to specify variations in mixing ratio for these two species in the lower thermosphere, although this could be done by varying the appropriate parameters with geographical and/or solar parameters.

The basic expansion formula (A22) used to express the exospheric temperature and other parameters as a function of local time, latitude, longitude, UT, $F_{10.7}$, and Ap has been augmented over that used in MSIS by higher order terms in the time independent and magnetic activity terms, a nonlinear (quadratic) term in mean $F_{10.7}$, a latitude dependent $F_{10.7}$ term, a seasonal dependent terdiurnal term, a seasonally dependent longitude-magnetic activity term, and optional magnetic activity terms using a condensed history of ap indices rather than a single daily average. The solar activity $F_{10.7}$ cross terms with the annual and daily variations (equations (A22b) and (A22c)) were chosen to make the relative annual and daily variation independent of short term solar activity. As previously, a number of other variations (such as the semiannual) are assumed to have no solar activity dependence as such a connection has not been established.

The model coefficients which specify the temperature and N_2 profile were divided into three groups by altitude and determined in three separate steps with iteration between them until so significant change in coefficients was noted. Interaction between coefficient groups was minimized by the selected altitude grouping as well as by the choice of temperature gradient at 120 km for a fitting parameter rather than using the Bates shape parameter. The exospheric temperature coefficients were determined using temperature and N_2 density data above 190 km. The temperature, temperature gradient, and N_2 density coefficients at 120 km were determined using temperature and N_2 or total density data primarily between 110 and 160 km with a small sampling of higher altitude data to facilitate compromise between the lower and upper thermosphere data sets. The mesopause temperature, height, and lower thermosphere shape coefficients were determined using temperature and N_2 or total density data between 85 and 120 km. Note that except for specifying the N_2 density at 120 km, the N_2 profile is almost entirely determined by integration of the temperature profile, since the difference between the diffusive and mixing profiles is very small and there are no other corrections.

The 120 km density coefficients for O_2, O, He, Ar, and H were determined using O_2 data above 150 km, O data above 190 km, He data above 190 km, and H data above 200 km. The flow effects coefficients (equations (A20) and (A21)) for O and O_2 were determined using O, O_2, and total density data below 190 km, including the O profile from the U.S. Standard Atmosphere and a constraint to minimize departures from hydrostatic equilibrium as applied by Hedin et al. [1983]. The flow effects coefficients for He were determined using He data below 190 km and for H using the results of Breig et al. [1976], Liu and Donahue [1974], and Anderson et al. [1980]. The 120 km density coefficients and flow effect coefficients for Ar were determined using data from all available altitudes.

TABLE 2a. Model Coefficients

	T_∞	He	O	O_2	Ar	H
Average	1.035E+03	2.556E+07	8.603E+10	3.165E+10	1.247E+09	2.185E+05
a_{10}	0.000E+00	-5.273E-02	-3.312E-02	0.000E+00	0.000E+00	-4.768E-02
a_{20}	2.394E-02	1.557E-03	-1.486E-01	1.999E-01	3.158E-01	-2.074E-01
a_{40}	-1.616E-03	-1.958E-01	-9.209E-02	0.000E+00	1.676E-01	-1.614E-01
a_{60}	1.631E-02	0.000E+00	0.000E+00	0.000E+00	0.000E+00	0.000E+00
f_{00}^{a1}	1.778E-03	-1.239E-03	5.235E-04	0.000E+00	0.000E+00	-6.316E-03
f_{00}^{a2}	-5.460E-06	3.098E-05	0.000E+00	0.000E+00	0.000E+00	4.094E-05
$\bar{f}_{00}^{a1}$	3.067E-03	3.226E-04	2.694E-03	-1.683E-03	0.000E+00	-1.368E-02
$\bar{f}_{00}^{a2}$	-6.771E-06	0.000E+00	-8.728E-06	0.000E+00	0.000E+00	0.000E+00
$\bar{f}_{20}^{a1}$	-4.669E-04	0.000E+00	0.000E+00	0.000E+00	0.000E+00	0.000E+00
$\bar{f}_{10}^{c}$	3.041E-03	-3.862E-03	0.000E+00	0.000E+00	0.000E+00	0.000E+00
$\bar{f}_{11}^{a}$	5.829E-03	1.844E-03	1.381E-03	0.000E+00	0.000E+00	-6.697E-03
k_{00}^{a}	5.975E-03	-1.019E-02	-7.432E-03	9.277E-03	1.490E-02	-2.210E-02
k_{20}^{a}	7.619E-03	-6.626E-02	-4.751E-02	1.756E-02	1.363E-02	-1.101E-02
k_{40}^{a}	4.038E-03	-1.072E-02	-1.543E-02	0.000E+00	0.000E+00	2.013E-02
k_{00}^{s}	2.004E-01	1.492E-01	2.071E-01	2.004E-01	2.004E-01	2.004E-01
k_{00}^{r}	1.937E-01	1.122E-01	1.320E-01	1.937E-01	1.937E-01	1.937E-01
c_{00}^{1}	1.098E-02	-8.332E-02	8.679E-02	5.307E-02	1.056E-01	5.530E-02
t_{00}^{c1}	3.762E+01	-1.578E+02	-1.763E+01	1.516E+01	2.889E+02	1.425E+02
c_{00}^{2}	1.424E-02	2.994E-01	1.348E-01	2.809E-02	3.413E-02	1.854E-02
c_{20}^{2}	0.000E+00	-5.526E-02	0.000E+00	0.000E+00	7.661E-02	0.000E+00
t_{00}^{c2}	1.304E+02	1.053E+02	1.059E+02	8.337E+01	1.363E+02	7.791E+01
c_{10}^{1}	-1.561E-01	1.389E+00	3.722E-01	6.394E-02	-4.299E-01	4.272E-01
c_{30}^{1}	-3.303E-02	1.569E-01	1.017E-02	0.000E+00	0.000E+00	1.180E-01
t_{10}^{c1}	-7.692E+00	-6.314E+00	-4.485E+00	-7.692E+00	-2.964E+01	-8.994E+00
c_{10}^{2}	-1.853E-02	6.918E-02	0.000E+00	0.000E+00	0.000E+00	0.000E+00
t_{10}^{c2}	6.667E+00	-2.181E+01	0.000E+00	0.000E+00	0.000E+00	0.000E+00
a_{11}	-1.120E-01	-1.104E-01	-6.652E-02	-3.207E-02	-2.364E-02	2.101E-01
a_{31}	-6.432E-03	-7.314E-03	-4.130E-03	0.000E+00	0.000E+00	2.937E-02
a_{51}^{1}	0.000E+00	-9.088E-03	0.000E+00	0.000E+00	0.000E+00	0.000E+00
c_{11}^{1}	0.000E+00	1.711E-02	0.000E+00	0.000E+00	0.000E+00	0.000E+00
c_{21}^{1}	1.146E-02	1.544E-02	2.637E-02	0.000E+00	4.231E-02	2.573E-02
b_{11}	-1.273E-01	3.712E-01	6.518E-02	4.736E-02	-2.172E-01	2.780E-01
b_{31}	1.191E-04	-1.679E-02	-3.165E-02	0.000E+00	0.000E+00	2.191E-02
b_{51}^{1}	0.000E+00	-2.416E-02	0.000E+00	0.000E+00	0.000E+00	0.000E+00
d_{11}^{1}	0.000E+00	-4.848E-02	0.000E+00	0.000E+00	0.000E+00	0.000E+00
d_{21}^{1}	-7.107E-03	1.272E-01	5.197E-02	0.000E+00	-4.073E-02	3.728E-02
a_{22}	-2.736E-03	7.146E-03	1.111E-02	-1.508E-02	-1.397E-02	1.720E-02
a_{42}^{1}	-1.175E-03	0.000E+00	3.585E-03	0.000E+00	0.000E+00	0.000E+00
c_{32}^{1}	3.948E-03	0.000E+00	0.000E+00	0.000E+00	0.000E+00	0.000E+00
b_{22}	9.537E-03	-1.945E-02	-2.866E-02	-4.651E-02	-7.119E-02	-1.111E-02
b_{42}^{1}	-1.087E-03	0.000E+00	-9.286E-04	0.000E+00	0.000E+00	0.000E+00
d_{32}^{1}	1.887E-03	0.000E+00	0.000E+00	0.000E+00	0.000E+00	0.000E+00

TABLE 2a. (continued)

	T_∞	He	O	O_2	Ar	H
a_{33_1}	8.287E-04	2.338E-03	8.635E-04	0.000E+00	-1.910E-03	-1.366E-03
c_{43_1}	-1.034E-04	0.000E+00	0.000E+00	0.000E+00	0.000E+00	0.000E+00
c_{63}	1.232E-04	0.000E+00	0.000E+00	0.000E+00	0.000E+00	0.000E+00
b_{33_1}	1.150E-03	-2.922E-03	-1.186E-03	0.000E+00	-3.621E-03	-2.501E-04
d_{43_1}	-2.196E-04	0.000E+00	0.000E+00	0.000E+00	0.000E+00	0.000E+00
d_{63}	-3.038E-06	0.000E+00	0.000E+00	0.000E+00	0.000E+00	0.000E+00

1.035E+03 = 1.035×10^3.

TABLE 2b. Model Coefficients (continued)

	T_∞	He	O	O_2	Ar	H
a_{21_0}	3.078E-03	-2.735E-02	-3.803E-03	-1.828E-02	-7.517E-04	-5.769E-03
a_{41_0}	2.418E-03	-2.262E-02	-4.561E-03	-8.966E-03	2.024E-02	-1.823E-02
a_{61_0}	5.230E-03	-5.924E-03	-1.025E-02	0.000E+00	9.298E-03	-1.236E-02
b_{21_0}	-2.636E-02	3.538E-02	7.889E-02	-6.266E-02	-3.216E-02	5.762E-02
b_{41_0}	-2.261E-03	3.645E-02	9.617E-03	-4.113E-02	-4.047E-02	5.666E-03
$b_{61_{a0}}$	3.664E-03	1.084E-02	-1.420E-02	0.000E+00	-2.404E-02	-1.707E-03
$\overline{f}_{21_1}$	5.521E-03	0.000E+00	2.770E-03	0.000E+00	0.000E+00	0.000E+00
a_{10_1}	-1.277E-02	1.828E-02	7.360E-03	0.000E+00	0.000E+00	-5.067E-02
a_{30_1}	-4.166E-02	1.516E-01	-1.680E-01	0.000E+00	0.000E+00	9.676E-02
$a_{50_{a1}}$	-2.886E-02	1.501E-01	-1.337E-01	0.000E+00	0.000E+00	1.232E-01
$t_{10_{a1}}$	2.940E+04	3.047E+04	-1.383E+04	0.000E+00	0.000E+00	-1.791E+04
$\overline{f}_{10_{a1}}$	5.264E-03	0.000E+00	5.056E-03	0.000E+00	0.000E+00	0.000E+00
r_{10_1}	-3.914E-01	-2.024E-01	-3.833E-01	0.000E+00	0.000E+00	0.000E+00
a_{1-1_1}	5.751E-04	-6.397E-04	0.000E+00	0.000E+00	0.000E+00	0.000E+00
a_{3-1_1}	3.794E-04	-5.674E-03	0.000E+00	0.000E+00	0.000E+00	0.000E+00
a_{5-1_1}	9.714E-04	0.000E+00	0.000E+00	0.000E+00	0.000E+00	0.000E+00
b_{1-1_1}	-4.516E-03	-2.494E-03	0.000E+00	0.000E+00	0.000E+00	0.000E+00
b_{3-1_1}	-2.752E-03	9.191E-03	0.000E+00	0.000E+00	0.000E+00	0.000E+00
b_{5-1_1}	1.116E-03	0.000E+00	0.000E+00	0.000E+00	0.000E+00	0.000E+00
a_{32_1}	5.116E-04	-7.638E-03	-3.885E-03	0.000E+00	1.125E-02	0.000E+00
$a_{52_{a1}}$	5.452E-04	-2.948E-03	-2.254E-03	0.000E+00	5.077E-03	0.000E+00
$t_{32_{a0}}$	9.608E+02	2.074E+03	-4.747E+03	0.000E+00	8.700E+03	0.000E+00
$k_{21_{a0}}$	1.894E-03	-1.290E-02	-3.518E-03	0.000E+00	7.982E-03	0.000E+00
$k_{41_{a0}}$	1.706E-03	-9.289E-04	-3.099E-03	0.000E+00	-1.578E-03	0.000E+00
$k_{61_{k0}}$	2.209E-04	1.590E-03	-2.128E-03	0.000E+00	-3.632E-03	0.000E+00
$\lambda_{21_{k1}}$	-6.790E+01	-8.340E+01	-4.855E+01	0.000E+00	-7.775E+01	0.000E+00
$r_{10_{a1}}$	-7.374E-01	-8.495E-01	0.000E+00	0.000E+00	-2.325E+00	0.000E+00
$k_{10_{a1}}$	4.702E-04	-9.808E-03	-8.592E-03	0.000E+00	-1.811E-02	7.561E-03
$k_{30_{a1}}$	1.291E-03	-1.167E-03	1.059E-02	0.000E+00	-1.223E-02	8.443E-03
$k_{50_{k1}}$	-3.879E-03	8.885E-03	0.000E+00	0.000E+00	1.728E-02	0.000E+00
t_{10}	1.297E+04	-9.288E+03	-9.541E+03	0.000E+00	1.873E+04	5.204E+03

TABLE 2b. (continued)

	T_∞	He	O	O_2	Ar	H
	Coefficients for Alternate Formulation With 3-Hour Indices					
k_{00}^{a}	7.634E-03	-8.191E-03	-1.412E-02	8.551E-03	2.013E-02	-2.834E-02
k_{20}^{a}	9.267E-03	-5.393E-02	-6.598E-02	2.474E-02	2.902E-02	-1.290E-02
k_{40}^{a}	2.703E-03	-1.493E-02	-1.388E-02	0.000E+00	0.000E+00	2.030E-02
k_{00}^{s}	2.379E-01	9.349E-02	3.413E-01	2.379E-01	2.379E-01	2.379E-01
k_{00}^{r}	1.723E-01	1.067E-01	1.088E-01	1.723E-01	1.723E-01	1.723E-01
$\beta_{00_{a0}}$	4.031E-05	3.785E-05	2.443E-05	-3.766E-05	2.741E-05	2.904E-05
$k_{21_{a0}}$	1.518E-03	-1.161E-02	-4.474E-03	0.000E+00	1.226E-02	0.000E+00
$k_{41_{a0}}$	1.728E-03	-4.628E-04	-5.619E-03	0.000E+00	-1.042E-03	0.000E+00
$k_{61_{a0}}$	6.895E-04	1.494E-03	-4.022E-03	0.000E+00	-6.110E-03	0.000E+00
$\lambda_{21_{k0}}$	-6.961E+01	-8.445E+01	-5.488E+01	0.000E+00	-8.386E+01	0.000E+00
$r_{10_{kl}}$	-3.833E-01	-7.892E-01	0.000E+00	0.000E+00	-1.780E+00	0.000E+00
$k_{10_{al}}$	2.262E-04	-8.700E-03	-1.104E-02	0.000E+00	-1.321E-02	7.843E-03
$k_{30_{al}}$	2.255E-03	1.292E-03	1.070E-02	0.000E+00	-9.172E-03	6.565E-03
$k_{50_{al}}$	-6.283E-03	9.562E-03	0.000E+00	0.000E+00	1.589E-02	0.000E+00
t_{10}^{kl}	1.221E+04	-8.632E+03	-1.067E+04	0.000E+00	2.138E+04	3.165E+03

TABLE 2c. Model Coefficients (continued)

	T_∞	He	O	O_2	Ar	H
Ω		6.711E-06	8.218E-02	2.683E-01	1.196E-02	2.329E-06
z_h		1.000E+02	1.050E+02	1.050E+02	1.050E+02	9.500E+01
z_1		1.247E+02	1.326E+02	1.152E+02	1.287E+02	1.223E+02
H_1		7.309E+00	4.026E+01	6.376E+00	1.108E+01	2.386E+01
z_2			7.166E+01			7.593E+01
H_2			8.161E+00			2.020E+00
R_2			-3.346E+01			-1.700E+01

TABLE 2d. Model Coefficients (continued)

	N_2	T_ℓ	z_o	T_o	T_R	T_ℓ'
Average	3.296E+11	3.807E+02	9.455E+01	1.806E+02	1.591E-01	1.466E+01
a_{20}	0.000E+00	0.000E+00	-2.637E-02	-7.325E-02	1.006E+00	1.377E-02
a_{40}	0.000E+00	0.000E+00	0.000E+00	0.000E+00	0.000E+00	9.448E-02
$\overline{f}_{00_{al}}$	1.670E-03	7.269E-04	1.924E-04	0.000E+00	0.000E+00	1.872E-03
$\overline{f}_{20_{a}}$	0.000E+00	0.000E+00	0.000E+00	0.000E+00	0.000E+00	2.039E-03
k_{00}^{a}	0.000E+00	5.751E-03	0.000E+00	0.000E+00	0.000E+00	0.000E+00
k_{20}^{a}	0.000E+00	7.278E-03	0.000E+00	0.000E+00	0.000E+00	0.000E+00
k_{00}^{s}	2.004E-01	2.004E-01	2.004E-01	2.004E-01	2.004E-01	2.004E-01
k_{00}^{r}	1.937E-01	1.937E-01	1.937E-01	1.937E-01	1.937E-01	1.937E-01
$c_{00_{cl}}$	7.413E-02	0.000E+00	0.000E+00	0.000E+00	0.000E+00	0.000E+00

TABLE 2d. (continued)

	N_2	T_ℓ	z_o	T_o	T_R	T_ℓ'
t_{00_2}	-2.211E+01	0.000E+00	0.000E+00	0.000E+00	0.000E+00	0.000E+00
$c_{00_{c2}}$	3.789E-02	1.229E-02	0.000E+00	0.000E+00	0.000E+00	0.000E+00
t_{00_1}	1.351E+02	7.147E+01	0.000E+00	0.000E+00	0.000E+00	0.000E+00
c_{10_1}	-9.980E-02	-3.530E-02	4.722E-02	1.276E-01	-5.880E-01	0.000E+00
$c_{30_{c1}}$	0.000E+00	0.000E+00	0.000E+00	8.189E-02	0.000E+00	0.000E+00
t_{10}	-7.692E+00	-7.692E+00	-7.692E+00	-7.692E+00	-7.692E+00	-7.692E+00
a_{11}	-1.576E-02	-1.106E-02	0.000E+00	0.000E+00	0.000E+00	0.000E+00
b_{11}	-2.674E-02	1.148E-02	0.000E+00	0.000E+00	0.000E+00	0.000E+00
a_{22}	1.851E-02	-8.919E-03	6.480E-03	9.927E-03	-6.160E-02	2.851E-02
a_{42_1}	6.376E-03	-2.630E-03	-2.568E-03	-5.105E-04	3.401E-02	7.593E-03
c_{32_1}	0.000E+00	0.000E+00	0.000E+00	0.000E+00	0.000E+00	-5.954E-03
c_{52}	0.000E+00	3.152E-04	1.314E-03	0.000E+00	0.000E+00	0.000E+00
b_{22}	-3.798E-02	1.275E-02	4.491E-03	1.578E-03	-1.082E-01	2.718E-03
b_{42_1}	3.335E-03	-6.404E-04	-4.101E-04	2.647E-03	-4.640E-02	1.922E-03
d_{32_1}	0.000E+00	0.000E+00	0.000E+00	0.000E+00	0.000E+00	6.611E-03
d_{52}	0.000E+00	2.593E-03	1.543E-03	0.000E+00	0.000E+00	0.000E+00
a33	1.406E-04	0.000E+00	0.000E+00	0.000E+00	0.000E+00	0.000E+00
b_{33}	-1.832E-03	0.000E+00	0.000E+00	0.000E+00	0.000E+00	0.000E+00
	Coefficients for Alternate Formulation With 3-hour indices					
k_{00_a}	0.000E+00	8.026E-03	0.000E+00	0.000E+00	0.000E+00	0.000E+00
k_{20_a}	0.000E+00	6.997E-03	0.000E+00	0.000E+00	0.000E+00	0.000E+00
k_{00_s}	2.379E-01	2.379E-01	2.379E-01	2.379E-01	2.379E-01	2.379E-01
k_{00_r}	1.723E-01	1.723E-01	1.723E-01	1.723E-01	1.723E-01	1.723E-01

When determining the exospheric temperature and 120-km density coefficients as described above, the nonmagnetic activity related coefficients were determined separately using quiet data only (Ap<10) and the longitude/UT coefficients for all but O_2 were also separated to reduce the number of parameters to be determined in one computer run.

The final model coefficients are given in Table 2 and a general summary of the model variations applicable to each geophysical parameter is given in Table 3. For the most part, only coefficients/terms are given in which the statistical error from the fit is estimated to be less than a third of the coefficient value. An exception was made for flow correction coefficients which are sometimes poorly determined, given a lack of constraining composition data in the lower thermosphere. The annual phases ($t_{10_{c1}}$) for O_2 and N_2 at 120 km, T_ℓ, T_ℓ', z_o, T_o, and T_r were assumed to have the same phase as for T_∞. Also, the magnetic activity coefficients k_{00_s} and k_{00_r} for O_2, Ar, and H at 120 km, T_ℓ, and $T_{\ell_{00}}$ were assumed to have the same value as for T_∞.

The average departures and standard deviations of the individual data subsets used in generating the model are given in Table 4, and these can be used as indicators of how well a data set can be represented by the model. For the most part the data set differences are not beyond reasonable bounds for the current state of the art in absolute thermospheric measurements. The (generally good) consistency between data sets and the model suggests a reasonable degree of confidence in the model as representative of typical thermospheric conditions. Although the various data sets are less tightly clustered about the model than previously, this is probably the result of using additional data sources. The most scatter between and within data sets occurs for the minor constituents helium and argon. Coverage is lacking at high latitudes for high solar activity, and so the model in this area is essentially extrapolation.

4. Results and Discussion

4.1. Mean, Time-Independent, and Solar Activity

The average global exospheric temperature ($F_{10.7}$ = 150) of 1035K is only 6K lower than MSIS, but the equatorial temperature is about 30K lower then before, and this is driven in part by the Atmospheric Explorer temperatures. The mean meridional profile near the equator thus has a dip at the equator, rather than a peak, and this trend shows up in comparing contour plots of

TABLE 3. Summary of Model Terms

	T_∞	He	O	O_2	Ar	H	N_2	T_ℓ	Z_o	T_o	T_R	T_ℓ'
Time independent	X	X	X	X	X	X			X	X	X	X
Solar activity	X	X	X	X	X	X	X	X	X			X
Symmetrical annual	X	X	X	X	X	X	X	X				
Symmetrical semiannual	X	X	X	X	X	X	X	X				
Asymmetrical annual	X	X	X	X	X	X	X	X	X	X	X	
Asymmetrical semiannual	X	X										
Diurnal	X	X	X	X	X	X	X	X				
Semidiurnal	X	X	X	X	X	X	X	X	X	X	X	X
Terdiurnal	X	X	X		X	X	X					
Magnetic activity	X	X	X	X	X	X		X				
Longitude	X	X	X	X	X	X						
UT	X	X	X			X						
UT/Longitude/Magnetic Activity	X	X	X		X	X						

TABLE 4a. Density Ratio to MSIS-83 for N_2, O, and He

		N_2			O			He		
Data Set	Altitude	Avg	SD	Pts	Avg	SD	Pts	Avg	SD	Pts
OGO 6 (MS)	400-700	1.08	0.27	659	1.15	0.16	1276	1.18	0.19	902
San Marco 3 (MS)	190-250	1.10	0.20	77	0.86	0.15	24	1.09	0.17	41
Aeros-A NATE (MS)	200-500	1.13	0.47	321	1.14	0.33	478	1.18	0.42	466
AE-C NATE (MS)	190-400	1.13	0.33	640	0.91	0.18	866	0.68	0.18	855
AE-C OSS (MS)	135-160+	0.97	0.15	440						
AE-C OSS (MS)	190-400	1.02	0.26	319	1.08	0.18	387	1.03	0.23	371
AE-D OSS (MS)	140-160+	0.99	0.16	184						
AE-D OSS (MS)	190-400	0.87	0.33	99	1.01	0.18	107	0.78	0.22	107
AE-E NACE (MS)	140-160+	1.01	0.13	815						
AE-E NACE (MS)	190-450	1.00	0.22	701	0.87	0.18	1019	0.93	0.17	1002
ESRO 4 (MS)	200-350	0.88	0.33	427	0.83	0.24	587	0.84	0.30	518
Rockets (MS)	100-120	0.83	0.36	35						
Rockets (MS)	110-160	0.92	0.30	28						
Rockets (MS)	190-300	0.90	0.32	39						
Arecibo (IS)	100-120	0.92	0.32	228						
Arecibo (IS)	110-135	1.14	0.51	109						

SD is standard deviation.
Avg is average.
Pts is number of points.

TABLE 4b. Density Ratio to MSIS-83 for Ar, O_2, and H

		Ar			O_2			H		
Data Set	Altitude	Avg	SD	Pts	Avg	SD	Pts	Avg	SD	Pts
San Marco 3 (MS)	190-250	2.05	0.29	75						
Aeros-A NATE (MS)	200-350	1.33	0.59	462						
AE-C NATE (MS)	250-350	1.36	0.38	339						
AE-C OSS (MS)	140-250	0.82	0.34	264	0.99	0.26	218			
AE-C EUVS (absorption)	100				0.99	0.24	121			
AE-C EUVS (absorption)	130				1.19	0.20	54			
AE-C EUVS (absorption)	150				1.04	0.31	130			
AE-D OSS (MS)	140-250	1.38	0.53	143	1.17	0.35	511			
AE-E NACE (MS)	140-300	1.02	0.21	641						
AE-E OSS (MS)	140-250				1.20	0.21	297			
AE-E EUVS (absorption)	100				0.95	0.31	249			
AE-E EUVS (absorption)	130				0.94	0.19	175			
AE-E EUVS (absorption)	150				0.80	0.16	296			
ESRO 4 (MS)	200-300	0.80	0.44	1042						
Rockets (MS)	140-200	0.91	0.48	63						
Rockets (MS)	130-220				0.91	0.30	278			
Rockets (absorp)	120-150				0.86	0.30	14			
AE-C BIMS (IMS)	200-500							1.01	0.26	2114
AE-C MIMS (IMS)	160-300							1.30	0.03	8
AE-E BIMS (IMS)	200-500							0.98	0.26	1577

TABLE 4c. Temperature Difference and Total Density Ratio to MSIS-83

Data Set	Altitude, km	Temperature Avg	Temperature SD	Temperature Pts	Density Avg	Density SD	Density Pts
Millstone Hill (IS)	100-120	1.	44.	882			
Millstone Hill (IS)	110-130	3.	42.	828			
Millstone Hill (IS)	exospheric	5.	45.	283			
St. Santin (IS)	exospheric	-4.	48.	176			
Arecibo (IS)	100-120	-3.	26.	697			
Arecibo (IS)	110-135	-2.	28.	782			
Arecibo (IS)	250-exospheric	13.	39.	182			
Jicamarca (IS)	exospheric	-26.	49.	33			
Malvern (IS)	240-400	-39.	68.	88			
AE-C NATE (MS)	135-160	-4.	60.	212			
AE-C NATE (MS)	190-300	-38.	103.	79			
AE-D NATE (MS)	140-160	13.	55.	95			
AE-D NATE (MS)	190-400	-29.	101.	84			
AE-E NATE (MS)	140-170	-8.	45.	419			
AE-E NATE (MS)	190-400	-23.	43.	335			
Rockets (MS)	100-120	-6.	30.	20			
Rockets (MS)	110-160	4.	49.	104			
Rockets (MS)	190-300	-24.	60.	31			
Rockets (gauge)	85-120	10.	25.	160	1.18	0.26	247
Rockets (gauge)	110-120	-22.	39.	17	1.01	0.20	58
Rockets (grenade)	85-110	0.	17.	309	1.00	0.17	310
Rockets (falling sphere)	85-120	1.	18.	140	1.13	0.26	201
Rockets (falling sphere)	110-120	-11.	33.	3	1.00	0.35	23

temperature for the revised model (Figures 1 and 2) with those in the original MSIS paper. The in situ temperature measurements from AE-C and AE-D provide the most direct opportunity to observe meridional gradients in temperature. However, the scatter is sufficiently large and the local time/seasonal coverage sufficiently sparse that details beyond a general dip in temperature from the poles to the equator cannot be easily confirmed. As in the J77 model [Jacchia, 1977] and suggested by incoherent scatter observations [McPherson and Rishbeth, 1979; Oliver, 1980] the temperature variation with $F_{10.7}$ is now nonlinear and is compared in Figure 3 to the MSIS and J77 models. A feature not previously included in thermospheric models is that the absolute pole to equator temperature difference increases as solar activity decreases. This effect is qualitatively consistent with the idea that polar heat input under quiet magnetic conditions, which keeps the poles warmer than the equator, is relatively constant over the solar cycle, while the solar EUV, which would produce a minimum at the poles, increases with solar activity. The total density variation with $F_{10.7}$ is seen in Figure 4, and it is noted that this variation, as well as absolute values, are closer to J77 than MSIS. While this may be somewhat accidental, and there is certainly not universal agreement in total density, agreement with J77 is often quite good in areas measured well by both satellite drag and mass spectrometer.

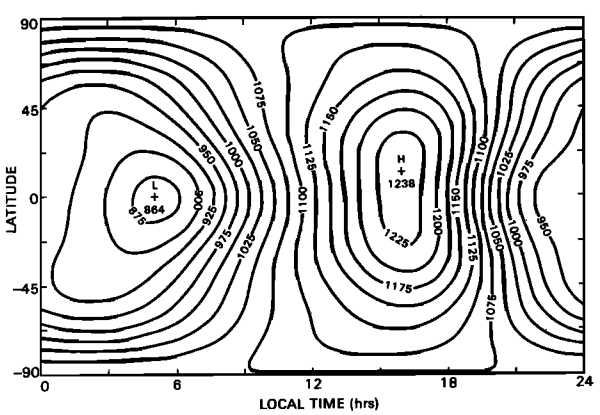

Fig. 1. Contour plot of exospheric temperature for the spring equinox, an $F_{10.7} = \overline{F}_{10.7}$ of 150, and an Ap of 4. Longitude/UT effects are not included.

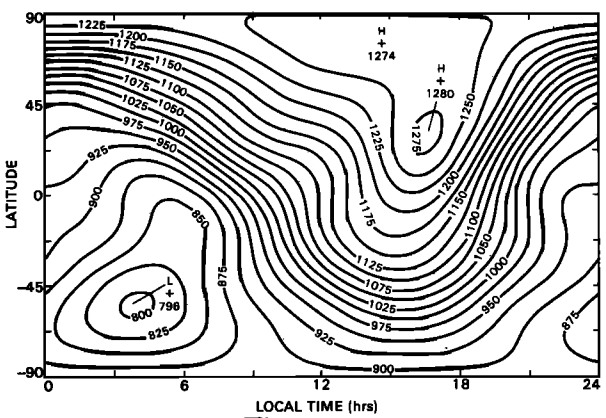

Fig. 2. Contour plot of exospheric temperature for the June solstice, an $F_{10.7} = \overline{F}_{10.7}$ of 150, and an Ap of 4. Longitude/UT effects are not included.

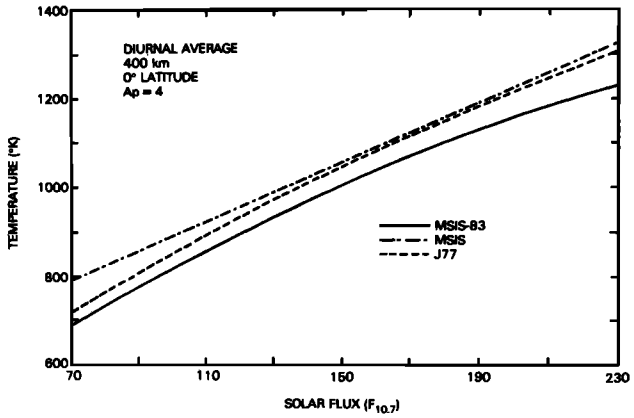

Fig. 3. Diurnal average temperature at 400 km versus solar flux ($F_{10.7} = \bar{F}_{10.7}$) for the September equinox at the equator, an Ap of 4, and longitude 0. The MSIS-83, original MSIS, and Jacchia [1977] (J77) models are shown.

The temperature and temperature gradient at 120 km are somewhat lower (and the N_2 density somewhat larger) than in the MSIS model but still in better agreement with incoherent scatter [Alcayde et al., 1979; Wand, 1983a] than J77 or the U.S. Standard Atmosphere, as seen in Figure 5. This change is one of the compromises necessary to match densities and temperatures over the extended altitude region of the model. The temperature at 120 km increases with $F_{10.7}$ in agreement with incoherent scatter [Wand, 1983a]. Data coverage near 120 km is still relatively poor compared to other altitudes and allows some flexibility in choosing density and temperature combinations needed to fit data at other altitudes.

The average height of the temperature minimum (mesopause) is 95 km with a temperature of 181K, and both these quantities decrease toward the poles. These results are in reasonable agreement with CIRA [Akedemie-Verlag, 1972], although the model mesopause is about 5 km higher than in CIRA. The annual average midnight temperature at 95 km, 40° latitude, and an $F_{10.7}$ of 150 is 184K, which is only a few degrees lower than that found by Hernandez [1976]. However, the MSIS-83 model does not have the strong inverse dependence of temperature with $F_{10.7}$ at this altitude found by Hernandez [1976], as this dependence is not consistent with either incoherent scatter [Alcayde et al., 1979] or rocket data.

The average densities at 120 km are all within 10% of the values in MSIS except for N_2 (up 17%) and H (up 24%). The lower thermosphere densities are quite close to those of the U.S. Standard Atmosphere, as seen in Figure 6. The N_2 density at 120 km increases, the O_2 density decreases with $F_{10.7}$; and the relative change in the O_2/N_2 ratio with $F_{10.7}$ is consistent with Kayser [1980]. The O_2 density at 120 km is roughly 25% higher than expected from diffusive equilibrium, and this is also consistent with Kayser [1980].

The effective molecular oxygen density at 120 km now increases by 34% toward the poles, rather than being constant as in MSIS. This effect combined with other problems in representing molecular oxygen variations (particularly magnetic activity) in the MSIS model may account in part for discrepancies noted by Torr et al. [1982], but the average density near 150 km has not changed significantly in this model over the older MSIS model. The suggestion by Torr et al. [1982] that model molecular oxygen densities be generally increased by 50% near 150 km is not consistent with the average value based on rockets and satellite data. However, there are significant differences between data sets, and there is considerable variation with geophysical conditions which must be recognized when applying chemistry calculations.

4.2. Yearly Variations

The global contours of exospheric temperature for solstice conditions are seen in Figure 2. The seasonal exospheric temperature and density variations of MSIS-83 are fairly similar to those of MSIS and J77, as seen in Figure 7, although the annual temperature variation predicted by J77 for midlatitudes peaks exactly at the solstices because it lacks a symmetrical annual and semiannual temperature variation. The seasonal temperature variation in the lower thermosphere is very similar to that of CIRA and shows the increasing height and temperature of the mesopause toward winter (Figure 8). While the phase of the seasonal variation in the lower thermosphere is in good agreement with measurements at St. Santin [Alcayde et al., 1979], analysis of Millstone Hill data [Wand, 1983a] shows a phase about 50 days later near 110 km.

The seasonal variation in molecular oxygen at 120 km is smaller than in MSIS but still with a winter maximum. On the basis of incoherent scatter measurements [Alcayde et al., 1974; Fontanari et al., 1982] it has been suggested that for high solar activity the seasonal variation of O_2 changes to a summer maximum four times the winter minimum. Unfortunately, at high solar activity there are few satellite measurements that bear on this question, but the available rocket measurements [Offermann, 1974] are not consistent with such a large seasonal variation at 120 or 200 km.

The seasonal variation of He at the poles is roughly a factor of 40 at low solar activity ($F_{10.7} = 75$) but, unlike MSIS, decreases in amplitude with increasing solar activity to

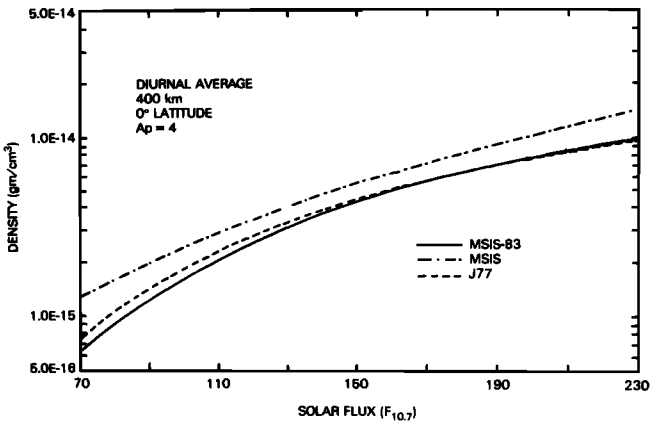

Fig. 4. Same as Figure 3 for total mass density.

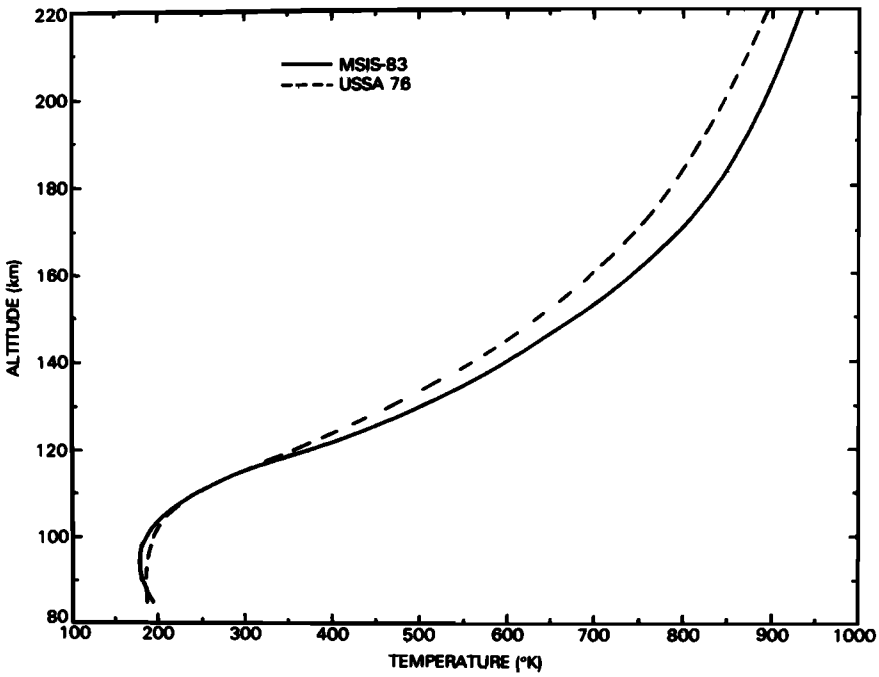

Fig. 5. Diurnal and annual average temperature versus altitude at latitude 45° for an $F_{10.7} = \overline{F}_{10.7}$ of 140 and an Ap of 4. The U.S. Standard Atmosphere 1976 profile is also shown. The arrow indicates the altitude z_a where the lower and upper thermosphere temperature profiles join.

roughly a factor of 18 at $F_{10.7} = 150$ and a factor of 10 at $F_{10.7} = 200$. This trend is consistent with differences between the OGO 6 and AE measurements. While these amplitudes are roughly consistent with the latest Jacchia [1977] model, which incorporated ESRO 4 results, they are much larger than the latest drag based model by Barlier et al. [1978] or the earlier drag based model by Jacchia [1971]. As pointed out by Barlier et al. [1978], the discrepancies in helium density are largest during local summer, when abundances are lowest. Referring to Trinks et al. [1977], Barlier et al. [1978] attribute this discrepancy to difficulties in measuring helium by mass spectrometer. However, the difficulties mentioned by Trinks et al. [1977]

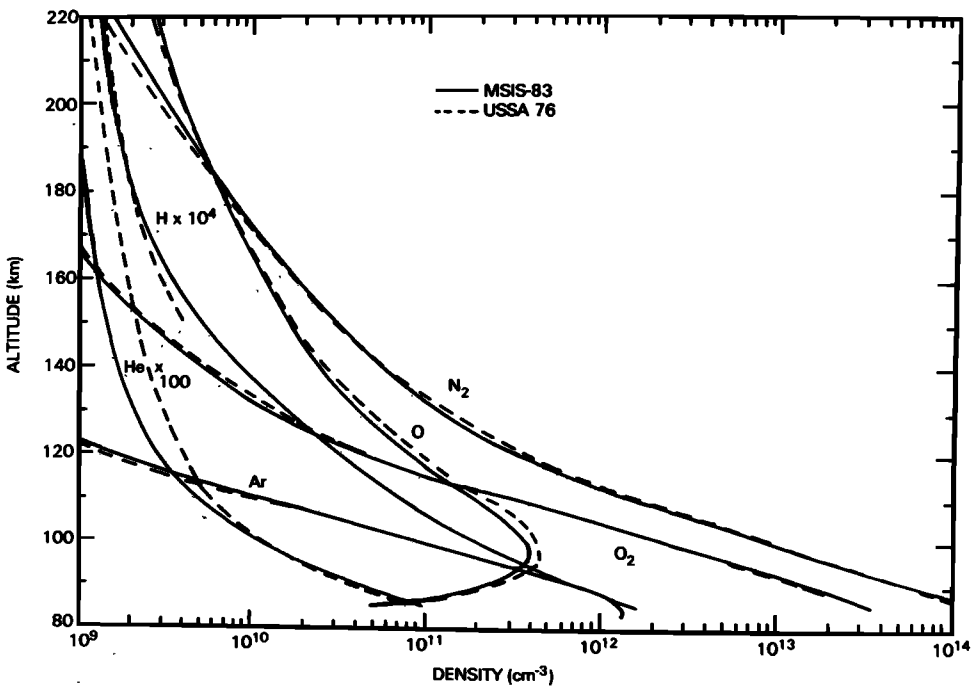

Fig. 6. Same as Figure 5 for N_2, O_2, O, He, Ar, and H density.

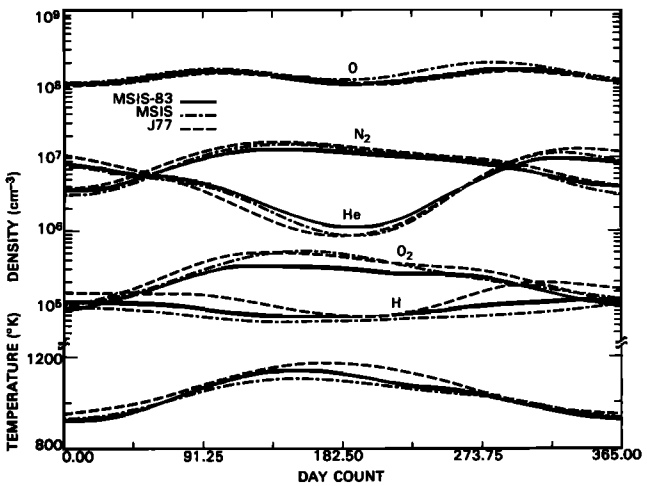

Fig. 7. Diurnal average temperature and density at 400 km versus day of year at 45° latitude, an $F_{10.7} = \overline{F}_{10.7}$ of 150, and an Ap of 4. The MSIS-83, original MSIS, and Jacchia [1977] models are shown.

relate to absolute calibration and not relative variations measured by a single instrument. It is highly unlikely that the direct in situ measurement would grossly overestimate the relative summer to winter variation. Rather, there may be problems in extracting the small helium abundance from drag measurements in summer when heavier constituents have increased in concentration.

The seasonal variation of argon at 120 km has a summer maximum, as did MSIS. J77, however, has no "seasonal latitudinal" component for argon and the net result is a winter maximum at 120 km.

4.3. Daily Variations

The equatorial daily variation of temperature and density at 400 km is illustrated in Figure 9 compared to MSIS and J77. Total density, N_2, and O variations are remarkably similar to J77 at this altitude. However, the helium amplitude, as in the seasonal variation, is underestimated by the drag analysis. In fact, this discrepancy gets increasingly worse at lower altitudes as the pseudotemperature approach of J77 is unable to represent the large diurnal helium amplitudes (Figure 10) seen down to 150 km [Hedin et al., 1978]. In total density variations the semidiurnal dominates the diurnal below 160 km. While this is a somewhat lower altitude than in MSIS, it is still reasonably consistent with observations by Sharp et al. [1978] and quite different in character from J77, where the diurnal is always dominant.

The semidiurnal tide in the lower thermosphere (below 120 km) has considerable structure both in latitude and altitude (see Forbes [1982] and references therein) which is beyond the scope of this model to include. However, the semidiurnal temperature amplitude in MSIS-83 does peak between 100 and 120 km, as found by incoherent scatter [Wand, 1983b] and with a phase in fairly reasonable agreement on average (see Figure 11). Discrepancies are greater in winter or summer and above 120 km. However, at altitudes above 120 km the model indicates that the diurnal temperature tide becomes comparable to the semidiurnal and this situation would complicate the analysis of the daytime incoherent scatter data. This model has a seasonal change in the phase of the semidiurnal around 115 km that is of opposite sign for Millstone Hill and Arecibo, similar to that found by Salah et al. [1977].

The terdiurnal composition variations at the equator [Hedin et al., 1980] are much better represented in the new model than by the MSIS model. The situation in temperature is less clear since the effect is very small and seems to be different between Millstone Hill and St. Santin.

The midnight temperature maximum [Spencer et al., 1979] is present only as a plateau region

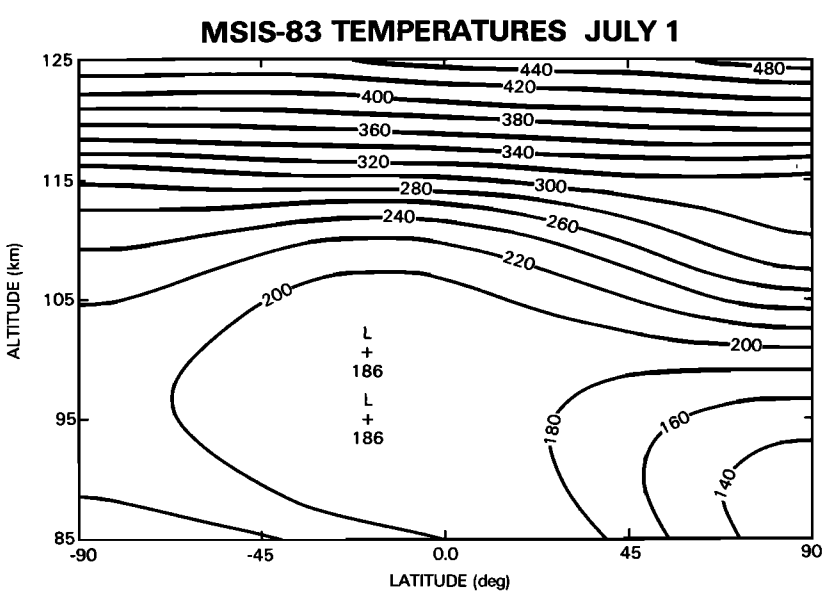

Fig. 8. Contour plot of diurnal average temperature on July 1 for an $F_{10.7} = \overline{F}_{10.7}$ of 150 and an Ap of 4.

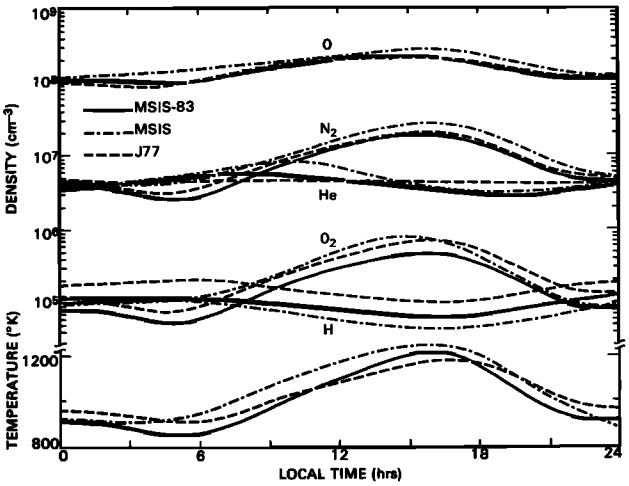

Fig. 9. Temperature and density at 400 km versus local time for the spring equinox at the equator, an $F_{10.7} = \overline{F}_{10.7}$ of 150, an Ap of 4, and longitude 0.

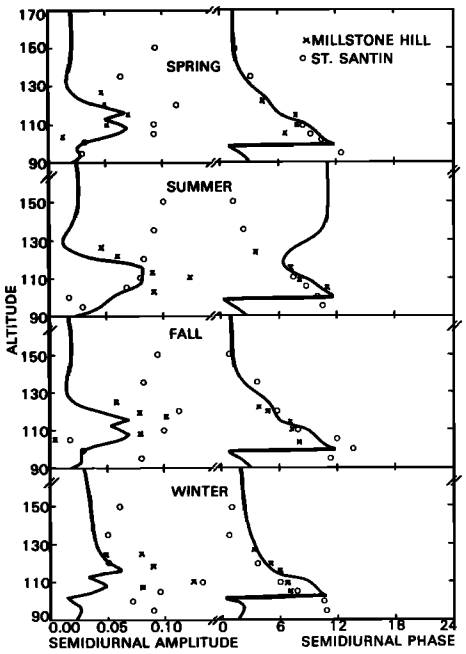

Fig. 11. Semidiurnal temperature amplitude and phase versus altitude at latitude 45° for the four seasons, an $F_{10.7} = \overline{F}_{10.7}$ of 120, and an Ap of 4. Also shown for comparison are measurements from Millstone Hill and St. Santin reported by Wand [1983 b].

around the equator near midnight in the contour plots of Figures 1 and 2. However, there is a seasonal variation in the semidiurnal and terdiurnal tides consistent with that described by Herrero et al. [1983], and the contours in Figure 2 show changes in the temperature gradient at the summer and winter terminator as discussed in that paper.

4.4. Magnetic Activity

The effective O_2 density at 120 km increases rather than decreases with magnetic activity and this effect is larger toward the poles. This O_2 variation is now qualitatively consistent with the reports by Parker and Stewart [1972], Nier et al. [1976], and Carver et al. [1978].

Modeling of magnetic storm effects in the neutral thermosphere requires both an index of energy deposition and some understanding of the response of the thermosphere to the energy deposition. While energy sources during magnetic storms have high spatial and temporal variability whose effects can in practice only be modeled in an average way, Mayr and Volland [1973] have demonstrated that the thermosphere reacts like a low pass filter to smooth out the response in temperature and density (but not in wind), and the response at any given time is the result of the prior history of energy deposition. The idea of summing over the recent history of energy input using an exponential decay factor was explored by Wydra [1975], Porter et al. [1981], and Hedin et al. [1981]. Recently, Nisbet et al. [1983] combined this idea with use of the auroral electrojet index and reported good results on a sample storm. However, it is not clear to what degree the favorable results could be attributed to the electrojet index or the summing procedure.

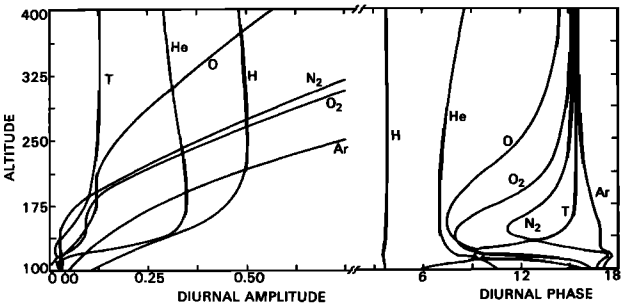

Fig. 10. Diurnal amplitude and phase of temperature and density versus altitude at the equator, an $F_{10.7} = \overline{F}_{10.7}$ of 70, and an Ap of 4.

As an alternate representation of storm effects the MSIS-83 model uses the 3-hour ap index in a summation formula (A24) to provide a more realistic description of the time history of an event. An example is seen in Figure 12 of the N_2 variation during a storm in 1976 (also discussed by Hedin et al. [1981]) as described using the daily Ap index and the summed 3-hour ap indices. The rise and fall of the density predicted using the summed three hour indices is much more representative of the data than either the prediction based on the daily index or the variation of the 3-hour index itself. For 1500 AE-C NATE density points in the interval shown in Figure 12, the variance of the N_2 and O density measurements from the model based on the summed 3-hour indices was a factor of two lower than for the model based on the daily Ap and 30% lower for He. On a longer time scale, however, since such large well defined storms are not the normal situation, the difference between the two storm models is much less on average. The time constants found for the storm response decay (β_{00}) are 6.9, 13.0, 11.4, 7.3, 7.4, 10.1, and 9.6 hours for exospheric temperature and the effective 120 km

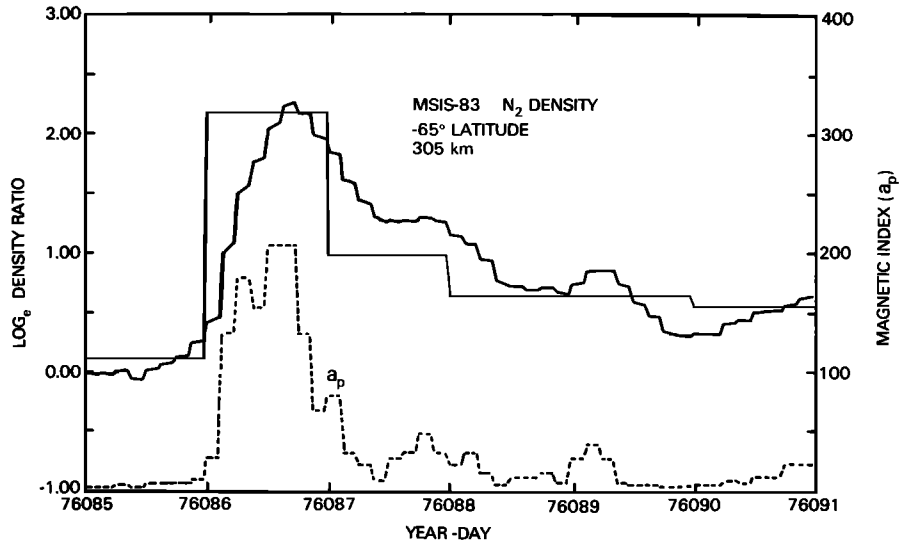

Fig. 12. Molecular nitrogen density versus day at latitude -65° and an altitude of 305 km for an actual storm in 1976 with $F_{10.7}$ near 72, comparing results using daily Ap index with that using a sum of ap indices (heavy line). Also shown are the 3-hour ap indices.

N_2, O, He, O_2, Ar, and H densities, respectively. The decay constant for oxygen is consistent with that found by Nisbet et al. [1983].

4.5. Longitude/UT

Oliver [1980] found a seasonal variation in the magnetic storm effect at Millstone Hill which apparently is not present at St. Santin, thus implying a longitude difference for this effect. This longitudinally dependent seasonal magnetic storm effect is included in the present model via the coefficient r_{10}^{kl} and was found significant for exospheric temperature, He, and H densities, although the temperature effect in the model (see Figure 13) is not as large as found in the Millstone Hill data. Some longitude/UT coefficients carried in the augmented MSIS model [Hedin et al., 1979] have been dropped as insignificant.

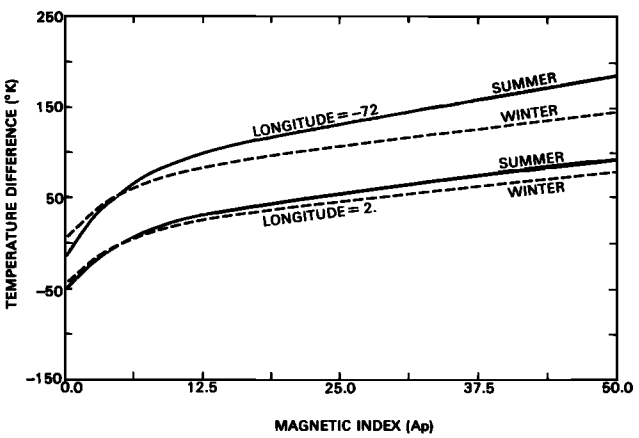

Fig. 13. Exospheric temperature versus Ap at latitude 45° and an $F_{10.7} = \overline{F}_{10.7}$ of 150, comparing summer and winter results for longitudes 2 and -72°.

4.6. Other Data

An extensive collection of temperatures obtained by Hernandez [1982] were not used in the current modeling effort, since they were about 100K above the MSIS model and it is not clear how they can be integrated with the other temperature data. These temperatures from Fritz Peak, based on line widths of atomic oxygen, are at the upper fringe of the temperatures measured by Millstone Hill. There is an even greater gap between these optical temperatures and the Atmospheric Explorer in situ temperatures, which are significantly below the MSIS model and still below the MSIS-83 model (Table 2). Density profiles near the equator from the AE-E satellite would not be consistent with higher model temperatures. Rocket profiles taken at midlatitudes tend to show lower rather than higher temperatures compared to the model. Other temperatures at midlatitudes, reported by Sipler et al. [1982] using optical techniques, are in reasonable agreement with MSIS, while measurements at the equator [Sipler et al., 1983] are several hundred degrees higher than models. These discrepancies with the optical measurements should be investigated further. If they are geophysical, as opposed to instrumental, then it may be indicative of strong spatial variations in temperature or mechanisms for production of the 6300 line different from those currently assumed and/or a lack of full thermalization of the emitting atoms.

5. Conclusion

The MSIS-83 empirical model presented in this paper provides a unified description of composition and temperature throughout the thermosphere while maintaining the same basic structure in the upper thermosphere as the previous MSIS model. The alternative magnetic storm representation in terms of summed 3-hour magnetic indices

should provide a better prediction of densities for specific events, such as rocket flights, occurring during a magnetic storm. The data base also includes a much wider range of solar activity than the previous MSIS model. While agreement among different data sets is generally remarkably good, there remain specific differences that need resolution. The remaining area of poorest data coverage at satellite altitudes is at high latitudes for high solar activity, while below 140 km the coverage for composition measurements is inadequate to specify in detail the transition from mixing to diffusive equilibrium as a function of local time, season, etc.

Appendix: Model Formulation

The temperature profile

$$T(z) = T_\infty - (T_\infty - T_\ell) \exp [-\sigma \xi (z, z_\ell)] \quad \text{(A1a)}$$

$$T(z) = 1/(1/T_o + T_B x^2 + T_C x^4 + T_D x^6) \quad z \geq z_a \quad \text{(A1b)}$$
$$z < z_a$$

and matching temperature and temperature gradient at z_a,

$$T_a = T(z_a) = T_\infty - (T_\infty - T_\ell) \exp [\sigma \xi (z_a, z_\ell)] \quad \text{(A2a)}$$

$$T_a' = T'(z_a) = (T_\infty - T_a) \sigma [R_p + z_\ell)/(R_p + z_a)]^2 \quad \text{(A2b)}$$

gives

$$T_D = 0.66666 \xi (z_o, z_a) T_a'/T_a^2 - 3.11111 (1/T_a - 1/T_o) + 7.11111 (1/T_{12} - 1/T_o) \quad \text{(A3a)}$$

$$T_C = \xi (z_o, z_a) T_a'/(2 T_a^2) - (1/T_a - 1/T_o) - 2 T_D \quad \text{(A3b)}$$

$$T_B = (1/T_a - 1/T_o) - T_C - T_D \quad \text{(A3c)}$$

$$x = [\xi (z, z_a) - \xi (z_o, z_a)]/\xi (z_o, z_a) \quad \text{(A3d)}$$

$$T_{12} = T_o + T_R (T_a - T_o) \quad \text{(A3e)}$$

$$\xi(z, z_\ell) = (z - z_\ell) (R_p + z_\ell)/(R_p + z) \quad \text{(A4a)}$$

$$\xi(z, z_a) = (z - z_a) (R_p + z_a)/(R_p + z) \quad \text{(A4b)}$$

$$\sigma = T_\ell'/(T_\infty - T_\ell) \quad \text{(A5)}$$

$$T_\ell' = \overline{T}_\ell' (1 + G(L)) \quad \text{(A6)}$$

$$T_\infty = \overline{T}_\infty [1 + G(L)] \quad \text{(A7)}$$

$$T_\ell = \overline{T}_\ell [1 + G(L)] \quad \text{(A8)}$$

$$T_o = \overline{T}_o [1 + G(L)] \quad \text{(A9)}$$

$$z_o = \overline{z}_o [1 + G(L)] \quad \text{(A10)}$$

$$T_R = \overline{T}_R [1 + G(L)] \quad \text{(A11)}$$

where

T ambient temperature, ^oK;
T_a, temperature at z_a, ^oK;
T_a' temperature gradient at z_a, ^oK/km;
T_{12} temperature at $(z_o + z_\ell)/2$, ^oK;
T_∞ average exospheric temperature (fitting parameter), ^oK
T_ℓ average temperature at z_ℓ (fitting parameter), ^oK;
T_o average mesopause temperature (fitting parameter), ^oK;
T_ℓ' average temperature gradient at z_ℓ (fitting parameter) ^oK/km;
T_R average mesopause shape parameter (fitting parameter);
z altitude, km;
z_ℓ 120 km;
z_a altitude of temperature profile junction (fitting parameter), 116.5 km;
$\overline{z}_o$ average mesopause height (fitting parameter), km;
R_p 6356.77 km.

The density profile is a meld of diffusive and mixing profiles multiplied by one or more factors $C_1 \ldots C_n$ to account for chemistry or dynamics flow effects

$$n(z, M) = [n_d (z, M)^A + n_m (z, M)^A]^{1/A} C_1(z) \ldots C_n(z) \quad \text{(A12a)}$$

$$A = M_h/(\overline{M}_o - M) \quad \text{(A12b)}$$

where

n ambient density, cm^{-3};
n_d diffusive profile;
n_m mixing profile;
$M_h = 28$;
$M_o = 28.95$,
M molecular weight of gas species.

The diffusive profile is

$$n_d (z, M) = n_\ell D (z, M) [T(z_\ell)/T(z)]^{1+\alpha} \quad \text{(A13)}$$

$$D(z, M) = D_B (z, M) \quad z \geq z_a \quad \text{(A14a)}$$

$$D(z, M) = D_B (z_a, M) \cdot \exp \{\gamma_1 [(x-1)/T_o + T_B (x^3 - 1)/3 + T_C (x^5-1)/5 + T_D (x^7-1)/7)\} \quad z < z_a \quad \text{(A14b)}$$

$$D_B (z, M) = [T (z_\ell)/T(z)]^{\gamma_2} \exp [-\sigma \gamma_2 \xi (z, z_\ell)] \quad \text{(A15)}$$

$$\gamma_2 = M g_\ell/(\sigma R_g T_\infty) \quad \text{(A16a)}$$

$$\gamma_1 = M g_a \xi (z_o, z_a)/R_g \quad \text{(A16b)}$$

$$g_\ell = g_s/(1 + z_\ell/R_p)^2 \quad \text{(A17a)}$$

$$g_a = g_s/(1 + z_a/R_p)^2 \quad \text{(A17b)}$$

$$n_\ell = \overline{n}_\ell \exp [G(L)] \quad \text{(A18)}$$

where $\overline{n}_\ell$ is the average density at z_ℓ (fitting parameter) per cubic centimeter, $g_s \cong 9.80665$ x

10^{-3} km/s^2, R_g = 8.314 x 10^{-3} g km^2/mols-s^2 - deg, α is the thermal diffusion coefficient, -0.4 for He and H, and zero otherwise.

The mixing profile with turbopause at z_h is

$$n_m(z, M) = n_\ell [D(z_h, M)/D(z_h, \bar{M}_o)] \cdot D(z, \bar{M}_o) [T(z_\ell)/T(z)] \quad (A19)$$

Simulation of chemistry and dynamic flow effects to produce an effective turbopause which provides a specified mixing ratio to N_2 is as follows:

$$C_1(z) = \exp\{R_1/[1 + \exp(z-z_1)/H_1]\} \quad (A20a)$$

$$R_1 = \log_e [\Omega\, n_m(z_\ell, M)/n_m(z_\ell, 28)] \quad (A20b)$$

where Ω is the mixing ratio relative to N_2 (fitting parameter for H and O), z_1 is the altitude at which log C_1 is R/2 (fitting parameter), and H_1 is the scale height for this correction (fitting parameter).

For O and H the above mixing ratio is conceived as that occurring without the loss/flow processes that produce the lower thermosphere peak. The peak is generated by a second factor:

$$C_2(z) = \exp\{R_2/[1 + \exp[z - z_2)/H_2]\} \quad (A21)$$

where R_2 is the density correction parameter (fitting parameter); z_2 is the altitude where log density correction is $R_2/2$ (fitting parameter), and H_2 is the scale height of this correction in kilometers (fitting parameter).

Expansion function for model quantities is as follows:

Time independent

$$G = a_{10} P_{10} + a_{20} P_{20} + a_{40} P_{40} + a_{60} P_{60}$$

Solar activity

$$+ \bar{f}_{00}^{a1} \Delta\bar{F} + \bar{f}_{00}^{a2} (\Delta\bar{F})^2 + f_{00}^{a1} \Delta F + f_{00}^{a2} (\Delta F)^2 + \bar{f}_{20}^{a1} P_{20} \Delta\bar{F}$$

Symmetrical annual

$$+ c_{00}^{1} \cos \Omega_d (t_d - t_{00}^{c1})$$

Symmetrical semiannual

$$+ (c_{00}^{2} + c_{20}^{2} P_{20}) \cos 2\Omega_d (t_d - t_{00}^{c2})$$

Asymmetrical annual (seasonal)

$$+ (c_{10}^{1} P_{10} + c_{30}^{1} P_{30}) F_1 \cos \Omega_d (t_d - t_{10}^{c1})$$

Asymmetrical semiannual

$$+ c_{10}^{2} P_{10} \cos 2\Omega_d (t_d - t_{10}^{c2})$$

Diurnal

$$+ [a_{11}P_{11} + a_{31}P_{31} + a_{51}P_{51} + (c_{11}{}^{1}P_{11} + c_{21}{}^{1}P_{21}) \cdot \cos \Omega_d (t_d - t_{10}^{c1})] F_2 \cos \omega\tau$$

$$+ [b_{11}P_{11} + b_{31}P_{31} + b_{51}P_{51} + (d_{11}{}^{1}P_{11} + d_{21}{}^{1}P_{21}) \cdot \cos \Omega_d (t_d - t_{10}^{c1})] F_2 \sin \omega\tau$$

Semidiurnal

$$+ [a_{22}P_{22} + a_{42}P_{42} + (c_{32}{}^{1}P_{32} + c_{52}{}^{1}P_{52}) \cos \Omega_d \cdot (t_d - t_{10}^{c1})] \cdot F_2 \cos 2\omega\tau + [b_{22}P_{22} + b_{42}P_{42} + (d_{32}{}^{1}P_{32} + d_{52}{}^{1}P_{52}) \cdot \cos \Omega_d (t_d - t_{10}^{c1})] F_2 \sin 2\omega\tau$$

Terdiurnal

$$+ [a_{33}P_{33} + (c_{43}{}^{1}P_{43} + c_{63}{}^{1}P_{63}) \cos \Omega_d (t_d - t_{10}^{c1})] \cdot F_2 \cos 3\omega\tau + [b_{33}P_{33} + (d_{43}{}^{1}P_{43} + d_{63}{}^{1}P_{63}) \cdot \cos \Omega_d (t_d - t_{10}^{c1})] F_2 \sin 3\omega\tau$$

Magnetic activity

$$+ (k_{00}^{a} + k_{20}^{a} P_{20} + k_{40}^{a} P_{40}) \Delta A$$

Longitudinal

$$+ (a_{21}{}^{0}P_{21} + a_{41}{}^{0}P_{41} + a_{61}{}^{0}P_{61}) (1 + \bar{f}_{21}^{a0} \Delta\bar{F}) \cos \lambda + (b_{21}{}^{0}P_{21} + b_{41}{}^{0}P_{41} + b_{61}{}^{0}P_{61}) (1 + \bar{f}_{21}^{a0} \Delta\bar{F}) \sin \lambda$$

UT

$$+ (a_{10}{}^{1}P_{10} + a_{30}{}^{1}P_{31} + a_{50}{}^{1}P_{50})(1 + \bar{f}_{10}^{a1} \Delta\bar{F}) \cdot (1 + r_{10}^{a1} P_{10}) \cos \omega'(t - t_{10}^{a1}) + (a_{1-1}{}^{1}P_{11} + a_{3-1}{}^{1}P_{31} + a_{5-1}{}^{1}P_{51}) \cos(\omega' t - \lambda) + (b_{1-1}{}^{1}P_{11} + b_{3-1}{}^{1}P_{31} + b_{5-1}{}^{1}P_{51}) \sin(\omega' t - \lambda) + (a_{32}{}^{1}P_{32} + a_{52}{}^{1}P_{52}) \cos[\omega'(t - t_{32}^{a1}) + 2\lambda]$$

UT/longitude/magnetic activity

$$+ [k_{21}^{a0} P_{21} + k_{41}^{a0} P_{41} + k_{61}^{a0} P_{61}] \cdot [1 + r_{10}^{k1} P_{10} \cos \Omega_d (t_d - t_{10}^{c1})] \Delta A \cos(\lambda - \lambda_{21}^{k0}) + [k_{10}^{a1} P_{10} + k_{30}^{a1} P_{30} + k_{50}^{a1} P_{50}] \Delta A \cdot \cos \omega'(t - t_{10}^{k1}) \quad (A22a)$$

$$F_1 = 1 + \bar{f}_{10}^{c} \Delta\bar{F} + f_{00}^{a1} \Delta F + f_{00}^{a2} (\Delta F)^2 \quad (A22b)$$

$$F_2 = 1 + \bar{f}_{11}^{a} \Delta\bar{F} + f_{00}^{a1} \Delta F + f_{00}^{a2} (\Delta F)^2 \quad (A22c)$$

where $\Delta F = F_{10.7} - \bar{F}_{10.7}$, $\Delta\bar{F} = \bar{F}_{10.7} - 150$, $F_{10.7}$ = 10.7 cm flux on previous day, 10^{-22} W m^{-2} Hz^{-1}, $\bar{F}_{10.7}$ is the average $F_{10.7}$ over three solar rotations (81 days) centered on required day, P_{nm} are the nonnormalized Legendre-associated functions, $\Omega_d = 2\pi/365$ day^{-1}, $\omega = 2\pi/24$ h^{-1}, $\omega' = 2\pi/86400$ s^{-1}, τ is local time in hours, t is UT in seconds, t_d is the day count in year, and λ is geographic longitude (eastward positive).

The magnetic activity factor is to be choosen from either

$$\Delta A = (Ap - 4) + (k_{00}^{r} - 1)\{Ap - 4$$

$$+ [\exp(-k_{00}^{s}(Ap - 4) - 1]/k_{00}^{s}\} \quad \text{(A23)}$$

where Ap is the daily magnetic index or

$$\Delta A = \{g(a_1) + [g(a_2) E(\beta) + g(a_3) E(\beta)^2 + g(a_4) E(\beta)^3 + (g(\bar{a}_{12}) E(\beta)^4 + g(\bar{a}_{30}) E(\beta)^{12} \cdot (1 - E(\beta)^8)/(1-E(\beta)) \cdot E(\beta)^{(t_m/10800-0.5)}]/\Sigma(\beta) \quad \text{(A24a)}$$

$$E(\beta) = \exp(-10800\,\beta) \quad \text{(A24b)}$$

$$\Sigma(\beta) = 1 + (1 - E(\beta)^{19}) \cdot E(\beta)^{(t_m/10800-.5)}/(1 - E(\beta)) \quad \text{(A24c)}$$

$$g(a) = (a - 4) + (k_{00}^{r} - 1)\{a - 4 + \{\exp(-k_{00}^{s}(a - 4)) - 1]/k_{00}^{s}\} \quad \text{(A24d)}$$

where β is the inverse of time constant for magnetic activity effect (fitting parameter) per second, $t_m = t \pmod{10800}$, a_1, a_2, a_3, a_4 are the 3-hour ap index for current time and 3, 6, and 9 hours before current time, $\bar{a}_{12}$ is the average of eight 3-hour ap indices from 12 to 35 hours prior to current time, and $\bar{a}_{36}$ is the average of eight 3-hour ap indices from 36 to 59 hours prior to current time.

Acknowledgements. The author is indebted to the many people who have gathered, reduced, and made available their data over the years. In particular, I would like to thank J. M. Forbes and M. E. Hagan for supplying post 1978 Millstone Hill exospheric temperature data in machine readable form, R. M. Harper for supplying a tape of Arecibo F region temperature data obtained after 1974, H. E. Hinteregger for supplying O_2 densities derived from AE EUVS measurements, D. C. Kayser for supplying available AE OSS O_2 data as well as a collection of mass spectrometer rocket data in machine readable form, P. H. McPherson and H. Rishbeth for supplying a tape of Malvern temperature data, R. A. Minzner for supplying a tape of his extensive compilation of rocket sounding results prior to 1973, G. P. Newton for supplying Thermosphere Probe rocket data in machine readable form, W. L. Oliver and R. H. Wand for supplying a tape of pre-1978 Millstone Hill two-pulse exospheric temperature data and E-region temperature data, N. W. Spencer and L. E. Wharton for supplying all available AE NATE temperature data, H. A. Taylor and H. C. Brinton for recalculating and supplying a tape of all available H densities based on AE BIMS, OSS, and NACE measurements, R. H. Wand and R. M. Harper for supplying a tape of Arecibo E region temperature and density data, and U. von Zahn and K. H. Fricke for supplying a tape of ESRO 4 composition data.

The Editor thanks U. von Zahn and W. L. Oliver for their assistance in evaluating this paper.

References

Ackerman, M., P. Simon, U. von Zahn, and U. Laux, Simultaneous upper air composition measurements by means of UV monochromators and mass spectrometers, J. Geophys. Res., 79, 4757-4764, 1974.

Akademie-Verlag, CIRA 1972, Berlin, 1972.

Alcayde, D., Diurnal and long-term behavior of the exospheric temperature as observed by incoherent scatter sounding in the F2 region, Radio Sci., 9, 239-245, 1974.

Alcayde, D., An analytic static model of temperature and composition from 20 to 2000 km altitude, Ann. Geophys., 37, 515-528, 1981.

Alcayde, D., P. Bauer, and J. Fontanari, Long-term variations of thermospheric temperature and composition, J. Geophys. Res., 79, 629-637, 1974.

Alcayde, D., J. Fontanari, G. Kockarts, P. Bauer, and R. Bernard, Temperature, molecular nitrogen concentration and turbulence in the lower thermosphere inferred from incoherent scatter data, Ann. Geophys., 35, 41-51, 1979.

Anderson, D. E., P. D. Feldman, E. P. Gentieu, and R. R. Meier, The UV dayglow 2, LY-alpha and LY-beta emissions and the H distribution in the mesosphere and thermosphere, Geophys. Res. Lett., 7, 529-532, 1980.

Barlier, F., C. Berger, J. L. Falin, G. Kockarts, and G. Thuillier, A thermospheric model based on satellite drag data, Ann. Geophys., 34, 9-24, 1978.

Bates, D. R., Some problems concerning the terrestrial atmosphere above the 100 km level, Proc. R. Soc. London, Ser. A, 253, 451-462, 1959.

Breig, E. L., W. B. Hanson, J. H. Hoffman and D. C. Kayser, In situ measurements of hydrogen concentration and flux between 160 and 300 km in the thermosphere, J. Geophys. Res., 81, 2677-2686, 1976.

Brinton, H. C., L. R. Scott, M. W. Pharo III, and J. T. Coulson, The Bennett ion mass spectrometer on Atmosphere Explorer-C and -E, Radio Sci., 8, 323-332, 1973.

Brinton, H. C., H. G. Mayr, and W. E. Potter, Winter bulge and diurnal variations in hydrogen inferred from AE-C composition measurements, Geophys. Res. Lett., 2, 389-392, 1975.

Carignan, G. R., and W. H. Pinkus, Ogo-F04 experiment description, Tech. Note 08041-3-T, Univ. of Mich., Ann Arbor, 1968.

Carver, J. H., L. A. Davis, B. H. Horton, and M. Ilyas, Ultraviolet extinction measurements of molecular oxygen density, J. Geophys. Res., 83, 4377-4380, 1978.

Chandra, S., and N. W. Spencer, Exospheric temperatures inferred from the Aeros A neutral composition measurement, J. Geophys. Res., 80, 3615-3621, 1975.

Cooley, J. E., and C. A. Reber, Neutral atmosphere composition measurement between 133 and 533 kilometers from the Geoprobe rocket mass spectrometer, Rep. NASA/GSFC X-621-69-260, 1969.

Fontanari, J., D. Alcayde, and P. Bauer, Seasonal changes in thermospheric molecular oxygen: A solar activity control, Geophys. Res. Lett., 9, 551-554, 1982.

Forbes, J. M., Atmospheric tides, 2, The solar and lunar semidiurnal components, J. Geophys. Res., 87, 5241-5252, 1982.

Harper, R. M., and R. H. Wand, Coordinated tidal observations at Arecibo, J. Atmos. Terr. Phys., 40, 887-890, 1978.

Hedin, A. E., H. G. Mayr, C. A. Reber, N. W. Spencer, and G. R. Carignan, Empirical model of global thermospheric temperature and composition based on data from the Ogo 6 quadrupole mass spectrometer, J. Geophys. Res., 79, 215-225, 1974.

Hedin, A. E., et al., A global thermospheric model based on mass spectrometer and incoherent scatter data, MSIS 1, N2 density and temperature, J. Geophys. Res., 82, 2139-2147, 1977a.

Hedin, A. E., C. A. Reber, G. P. Newton, N. W. Spencer, H. C. Brinton, H. G. Mayr, and W. E. Potter, A global thermospheric model based on mass specrometer and incoherent scatter data, MSIS 2, Composition, J. Geophys. Res., 82, 2148-2156, 1977b.

Hedin, A. E., N. W. Spencer, H. G. Mayr, I. Harris, and H. S. Porter, Direct evidence of transport processes in the thermospheric diurnal tide, J. Geophys. Res., 83, 3355-3357, 1978.

Hedin, A. E., C. A. Reber, N. W. Spencer, H. C. Brinton, and D. C. Kayser, Global model of longitude/UT variations in thermospheric composition and temperature based on mass spectrometer data, J. Geophys. Res., 84, 1-9, 1979.

Hedin, A. E., N. W. Spencer, and H. G. Mayr, The semidiurnal and terdiurnal tides in the equatorial thermosphere from AE-E measurements, J. Geophys. Res., 85, 1787-1791, 1980.

Hedin, A. E., N. W. Spencer, H. G. Mayr, and H. S. Porter, Semiempirical modeling of thermospheric magnetic storms, J. Geophys. Res., 86, 3515-3518, 1981.

Hedin, A. E., H. B. Niemann, W. T. Kasprzak, and A. Seiff, Global empirical model of the Venus thermosphere, J. Geophys. Res., 88, 73-83, 1983.

Hernandez, G., Lower-thermosphere temperatures determined from the line profiles of the OI 17,924-K (5577 A) emission in the night sky, 1, Long-term behavior, J. Geophys. Res., 81, 5165-5172, 1976.

Hernandez, G., Mid-latitude thermospheric neutral kinetic temperatures, 1, Solar, geomagnetic and long-term effects, J. Geophys. Res., 87, 1623-1632, 1982.

Herrero, F. A., H. G. Mayr, and N. W. Spencer, Latitudinal (seasonal) variations in the thermospheric midnight temperature maximum: A tidal analysis, J. Geophys. Res., 88, 7225-7235, 1983.

Hinteregger, H. E., D. E. Bedo, and J. E. Manson, The EUV spectrophotometer on Atmosphere Explorer, Radio Sci., 8, 349-359, 1973.

Hinteregger, H. E., and L. M. Chaikin, EUV absorption analysis of thermospheric structure from AE-satellite observations of 1974-1976, Space Res., 17, 525-532, 1977.

Jacchia, L. G., Revised static models of the thermosphere and exosphere with empirical temperature profiles, Spec. Rep. 332, Smithsonian Astrophys. Observ., Cambridge, Mass., 1971.

Jacchia, L. G., Thermospheric temperature, density, and composition: new models, Spec. Rep. 375, Smithsonian Astrophys. Observ., Cambridge, Mass., 1977.

Jacchia, L. G., J. W. Slowey, and U. von Zahn, Temperature, density, and composition in the disturbed thermosphere from ESRO 4 gas-analyzer measurements: A global model., J. Geophys. Res., 82, 684-688, 1977.

Kayser, D. C., Solar flux variation of the thermospheric molecular oxygen density, J. Geophys. Res., 85, 695-702, 1980.

Laux, U., and U. von Zahn, Longitudinal variations in thermospheric composition under geomagnetically quiet conditions, J. Geophys. Res., 84, 1942-1946, 1979.

Liu, S. C., and T. M. Donahue, Realistic model of hydrogen constituents in the lower atmosphere and escape flux from the upper atmosphere, J. Atmos. Sci., 31, 2238-2242, 1974.

Mayr, H. G., and H. Volland, Magnetic storm characteristics of the thermosphere, J. Geophys. Res., 78, 2251-2264, 1973.

McClure, J. P., Thermospheric temperature variations inferred from incoherent scatter observations, J. Geophys. Res., 76, 3106-3115, 1971.

McPherson, P. H., and H. Rishbeth, Thermospheric temperatures over Malvern: a comparison of incoherent scatter data with two global thermospheric models, J. Atmos. and Terr. Phys., 41, 1021-1029, 1979.

Minzner, R. A., P. Morgenstern, P., and S. M. Mello, Tabulations of atmospheric density, temperature and pressure from 437 rocket and optical-probe soundings during the period 1947 to early 1965, Rep. TR-67-10-N, GCA Corporation, Bedford, Mass., 1967.

Newton, G. P., W. T. Kasprzak, and D. T. Pelz, Equatorial composition in the 137- to 225-km region from San Marco 3 mass spectrometer, J. Geophys. Res., 79, 1929-1941, 1974.

Newton, G. P., W. T. Kasprzak, S. A. Curtis, and D. T. Pelz, Local time variation of equatorial thermospheric composition determined by the San Marco 3 Nace, J. Geophys. Res., 80, 2289-2299, 1975.

Nier, A. O., W. E. Potter, D. R. Hickman, and K. Mauersberger, The open-source neutral mass spectrometer on Atmosphere Explorer-C, -D, -E, Radio Sci., 8, 271-276, 1973.

Nier, A. O., W. E. Potter, and D. C. Kayser, Atomic and molecular oxygen densities in the lower thermosphere, J. Geophys. Res., 81, 17-24, 1976.

Nisbet, J. S., C. Stehle, and E. Bleuler, Initial tests of an index based on AL values for modeling magnetic storm related perturbations of the thermosphere, J. Geophys. Res., 88, 2175-2180, 1983.

Offermann, D., Composition variations in the lower thermosphere, J. Geophys. Res., 79, 4281-4293, 1974.

Oliver, W. L., Improved Millstone Hill exospheric temperature measurements: evidence for a seasonal variation of the magnetic activity effect, J. Geophys. Res., 85, 4237-4247, 1980.

Parker, A. E., and K. H. Stewart, Measurements of molecular oxygen in the thermosphere, J. Atmos. Terr. Phys., 34, 1223-1232, 1972.

Pelz, D. T., C. A. Reber, A. E. Hedin, and G. R. Carignan, A neutral atmosphere composition experiment for the Atmosphere Explorer-C, -D, -E, Radio Sci., 8, 277-285, 1973.

Porter, H. S., H. G. Mayr and A. E. Hedin, An analytic formulation for heating source memory

in the thermospheric composition, J. Geophys. Res., 86, 3555-3560, 1981.
Reber, C. A., R. A. Minzner, and F. T. Huang, Definition of model II, in The 1976 Standard Atmosphere Above 86-km Altitude, edited by R. A. Minzner, Rep. NASA SP-398, Washington, D.C., 1976.
Salah, J. E., and J. V. Evans, Measurements of thermospheric temperatures by incoherent scatter radar, Space Res., 8, 267-286, 1973.
Salah, J. E., R. H. Wand, and R. Bernard, Comparison of simultaneous tidal observations by incoherent scatter radars, Ann. Geophys., 33, 95-102, 1977.
Sharp, L. R., D. R. Hickman, C. J. Rice, and J. M. Straus, The altitude dependence of the local time variation of thermospheric density, Geophys. Res. Lett., 5, 261-263, 1978.
Sipler, D. P., B. B. Luokkala, and M. A. Biondi, Fabry-Perot determinations of midlatitude F-Region neutral winds and temperature from 1975 to 1979, Planet. Space Sci., 20, 1025-1032, 1982.
Sipler, D. P., M. A. Biondi, and R. G. Roble, F-Region neutral winds and temperatures at equatorial latitudes: Measured and predicted behavior during geomagnetically quiet conditions, Planet. Space Sci., 31, 53-66, 1983.
Spencer, N. W., G. P. Newton, G. R. Carignan, and D. R. Taeusch, Thermospheric temperature and density variations with increasing solar activity, Space Res., 10, 389-412, 1969.
Spencer, N. W., H. B. Niemann, and G. R. Carignan, The neutral-atmosphere temperature instrument, Radio Sci., 8, 284-296, 1973.
Spencer, N. W., D. T. Pelz, H. B. Niemann, G. R. Carignan, and J. R. Caldwell, The neutral atmosphere temperature experiment, J. Geophys., 40, 613, 1974.
Spencer, N. W., G. R. Carignan, H. G. Mayr, H. B. Niemann, R. F. Theis, and L. E. Wharton, The midnight temperature maximum in the earth's equatorial thermosphere, Geophys. Res. Lett., 6, 444-446, 1979.
Theon, J. S., W. S. Smith, J. F. Casey, and B. R. Kirkwood, The mean observed meteorological structure and circulation of the stratosphere and mesosphere, NASA Tech. Rep. TR R-375, 1972.
Torr, M. R., D. G. Torr, R. Carter, and D. Kayser, Thermospheric molecular oxygen, J. Geophys. Res., 87, 1727-1732, 1982.
Trinks, H., and U. von Zahn, The Esro 4 gas analyzer, Rev. Sci. Instrum., 46, 213-217, 1975.
Trinks, H., U. von Zahn, C. A. Reber, A. E. Hedin, N. W. Spencer, D. Krankowsky, P. Lammerzahl, D. C. Kayser, and A. O. Nier, Intercomparison of neutral composition measurements from the satellites ESRO 4, AEROS A, AEROS B and Atmosphere Explorer C, J. Geophys. Res., 82, 1261-1265, 1977.
Trinks, H., D. Offermann, U. von Zahn, and C. Steinhauer, Neutral composition measurements between 90- and 220-km altitude by rocket-borne mass spectrometer, J. Geophys. Res., 83, 2169-2176, 1978.
Waldteufel, P., and L. Cogger, Measurements of the neutral temperatures at Arecibo, J. Geophys. Res., 76, 5322-5336, 1971.
Walker, J. C. G., Analytic representation of upper atmosphere densities based on Jacchia's static diffusion models, J. Atmos. Sci., 22, 462,1965.
Wand, R. H., Lower thermospheric structure from Millstone Hill incoherent scatter radar measurements, 1, Daily mean temperature, J. Geophys. Res., 88, 7201-7209, 1983a.
Wand, R. H., Lower thermospheric structure from Millstone Hill incoherent scatter radar measurements, 2, Semidiurnal temperature component, J. Geophys. Res., 88, 7211-7224, 1983b.
Williams, P. J. S., and G. N. Taylor, The UK incoherent scatter radar, Radio Sci., 9, 85-88, 1974.
Wydra, B. J., Global exospheric temperatures and densities under active solar conditions, Sci. Rep. 436, Penn. State Univ., University Park, 1975.
von Zahn, U., W. Kohnlein, K. H. Fricke, U. Laux, H. Trinks, and H. Volland, Esro 4 model of global thermospheric composition and temperatures during times of low solar activity, Geophys. Res. Lett., 4, 33-36, 1977.

A. E. Hedin, Goddard Space Flight Center, Code 961, Greenbelt, MD 20771.

(Received June 30, 1983;
revised August 22, 1983;
accepted August 23, 1983.)